

Polarization evolution characteristics of focused hybridly polarized vector fields

Bing Gu · Yang Pan · Guanghao Rui ·
Danfeng Xu · Qiwen Zhan · Yiping Cui

Received: 22 April 2014 / Accepted: 30 July 2014 / Published online: 14 August 2014
© Springer-Verlag Berlin Heidelberg 2014

Abstract We investigate the focusing property and the polarization evolution characteristics of hybridly polarized vector fields in the focal region. Three types of hybridly polarized vector fields, namely azimuthal-variant hybridly polarized vector field, radial-variant hybridly polarized vector field, and spatial-variant hybridly polarized vector field, are experimentally generated. The intensity distributions and the polarization evolution of these hybridly polarized vector fields focused under low numerical aperture (NA) are experimentally studied and good agreements with the numerical simulations are obtained. The three-dimensional (3D) state of polarization and the field distribution within the focal volume of these hybridly polarized vector fields under high-NA focusing are studied numerically. The optical curl force on Rayleigh particles induced by tightly focused hybridly polarized vector fields, which results in the orbital motion of trapped particles, is analyzed. Simulation results demonstrate that polarization-only modulation provided by the hybridly polarized vector field allows one to control both the intensity distribution and 3D elliptical polarization in the focal region, which may find interesting applications in particle trapping, manipulation, and orientation analysis.

1 Introduction

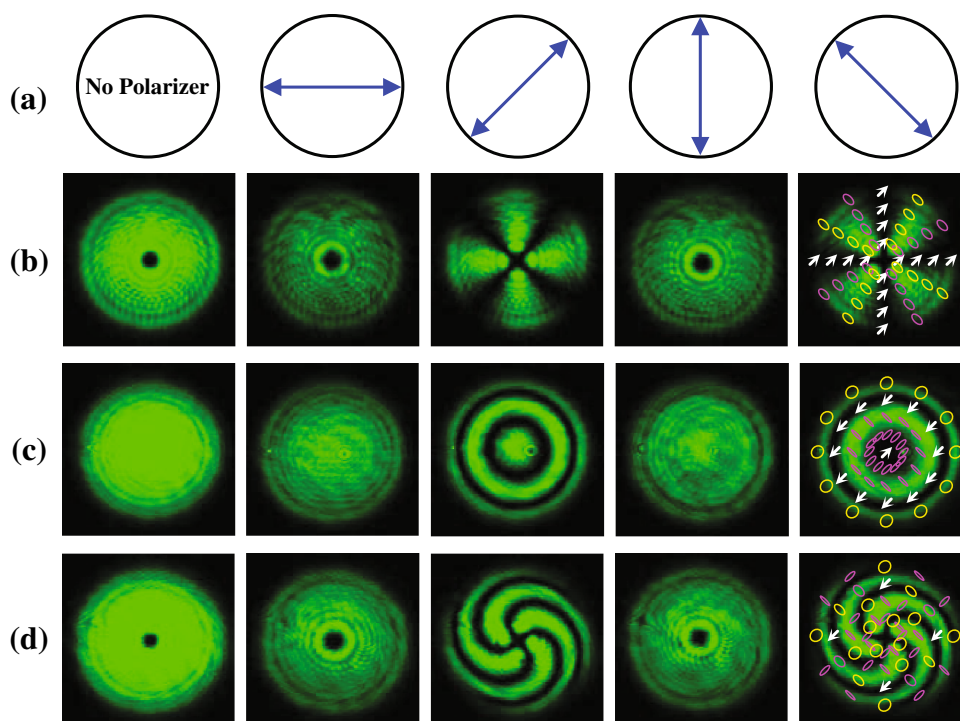
Optical vector fields with spatially variant state of polarization (SoP) have attracted increasing attention due to their broad potential applications in various areas, including optical tweezers [1], micromechanics [2], nonlinear optics [3, 4], quantum optics [5], atom optics [6], and optical microscopy [7, 8]. There have been many works that dealt with the generation, propagation, and applications of different types of vector fields, such as the radially and azimuthally polarized beams [9], cylindrical vector fields [10], and spatial-variant linearly polarized vector field [11]. By manipulating the amplitude, phase and polarization of vector fields as illumination, researchers have created a wide range of novel focal field distributions, such as optical bottle [12], optical cage [13, 14], optical chain [15], optical needle [16–18], and longitudinal bifocusing [19]. It should be noted that the SoP distribution of the above-mentioned vector fields can be characterized by local linear polarization with spatially varying orientation in the cross section of the field.

Recently, hybridly polarized vector fields with spatially variant hybrid SoP (including linear, elliptical, and circular polarizations) in the cross section of the field have been generated by transmitting radially polarized light through a wave plate [20] and a common path interferometer [21]. Interests in hybridly polarized vector fields have been prompted by their intriguing applications in particle orientation analysis [6, 20], laser material processing [22], controllable field collapse [4], and optical trapping [23, 24]. The focusing property of the hybridly polarized vector fields differs from that of the spatially variant linearly polarized vector fields. For instance, the tightly focused radial-variant hybridly polarized vector field has been studied to induce orbital motion of the isotropic particles [23], convert the radial-variant spin angular momentum

B. Gu · Y. Pan · D. Xu · Y. Cui (✉)
Advanced Photonics Center, Southeast University,
Nanjing 210096, China
e-mail: cyp@seu.edu.cn

G. Rui · Q. Zhan
Electro-Optics Program, University of Dayton, 300 College
Park, Dayton, OH 45469-2951, USA
e-mail: qzhan1@udayton.edu

Fig. 1 Intensity patterns without and with a linear polarizer for **b** the azimuthal-variant hybridly polarized vector field ($m = 2$ and $n = 0$), **c** the radial-variant hybridly polarized vector field ($m = 0$ and $n = 1$), and **d** the spatial-variant hybridly polarized vector field ($m = 2$ and $n = 1$). The *first row* illustrates the directions of the linear polarizer. The *fifth column* shows schematics of SoP (purple RH polarization; yellow LH polarization; white arrows linear polarization). The dimension for all of these images is $4 \text{ mm} \times 4 \text{ mm}$



into the radial-variant orbital angular momentum [25], and generate a super-long optical needle with the aid of an annular lens [17]. Li et al. [4] demonstrated the controllable collapse of the focused azimuthal-variant hybridly polarized vector field in a self-focusing Kerr medium. Lerman et al. [20] and Hu et al. [26] investigated the tight focusing properties of the azimuthal-variant hybridly polarized vector fields, respectively.

In this work, we investigate both theoretically and experimentally the focusing properties and the polarization evolution characteristics of hybridly polarized vector fields in the focal region. Three types of hybridly polarized vector fields, namely azimuthal-variant hybridly polarized vector field, radial-variant hybridly polarized vector field, and spatial-variant hybridly polarized vector field, are generated experimentally. The intensity distributions and the evolution of polarization through the focal region of these hybridly polarized vector fields under both low and high numerical aperture (NA) focusing conditions are studied in details. The optical curl force on Rayleigh particles induced by tightly focused hybridly polarized vector fields, which results in the orbital motion of trapped particles, is analyzed. Polarization-only modulation provided by the hybridly polarized vector field allows one not only to control the overall intensity distribution but also to manipulate the polarization distribution with 3D orientation and spatially variant ellipticity in the focal region, which may find interesting applications in trapping, manipulation, and orientation analysis.

2 Generation of hybridly polarized vector fields

The electric field distribution of a hybridly polarized vector field can be expressed as [25]

$$\mathbf{E}(r, \phi) = A_0 \text{circ}(r/r_0) [\exp(i\delta)\hat{e}_x + \exp(-i\delta)\hat{e}_y] \quad (1)$$

with $\delta = m\phi + 2n\pi r^2/r_0^2 + \varphi_0$. Here, the nonnegative integer m is the azimuthal index, the arbitrary number n is the radial index, φ_0 is the initial phase, r_0 is the radius of the vector field, A_0 is a constant, $\text{circ}(\cdot)$ is the circular function, r is the polar radius, and ϕ is the azimuthal angle. \hat{e}_x and \hat{e}_y are the unit vectors in the Cartesian coordinate system (x, y) . In general, hybridly polarized vector fields can be classified into three categories, namely azimuthal-variant hybridly polarized vector field ($m \neq 0, n = 0$), radial-variant hybridly polarized vector field ($m = 0, n \neq 0$), and spatial-variant hybridly polarized vector field ($m \neq 0, n \neq 0$). Note that the spatial-variant hybridly polarized vector field has the spatial distribution of hybrid SoP with simultaneous azimuthal and radial variations.

The azimuthal-variant hybridly polarized vector field has been generated by a common path interferometer implemented with the use of a spatial light modulator (SLM) [21]. Following the same method presented by Wang et al. [21] and using a 532-nm CW laser beam, three types of hybridly polarized vector fields with $\varphi_0 = 0$ are generated (shown in Fig. 1). Note that the additional phase in a computer-controlled SLM is set as $\delta(r, \phi) = m\phi + 2n\pi r^2/r_0^2 + \varphi_0$, whereas $\delta(\phi) = m\phi + \varphi_0$

was used for the azimuthal-variant hybridly polarized vector field reported previously [21]. The radius of all the generated vector fields is measured to be $r_0 = 1.7 \pm 0.1$ mm. Without the use of a linear polarizer, the generated vector fields have no distinction in intensity patterns except for the central dark spots when $m \neq 0$. These central dark spots arise from the singularity in the polarization orientation at the center of the vector fields, in contrary to the case for a radial-variant hybridly polarized vector field that has a well-defined polarization direction in the center. Interestingly, the intensity patterns for three types of hybridly polarized vector fields after passing a horizontal or a vertical linear polarizers are also undistinguishable, except that the overall intensities are reduced to a half of that prior to the polarizer. However, the intensity patterns after a $\pi/4$ and $3\pi/4$ linear polarizers appear as the fanlike extinction for the azimuthal-variant hybridly polarized vector field [21], the homocentric extinction rings for the radial-variant hybridly polarized vector field [23], and the spiral structure for the spatial-variant hybridly polarized vector field. In contrast, for the spatial-variant linearly polarized vector field, the intensity patterns behind the linear polarizer are always distinguishable [21, 27]. As illustrated in the fifth column of Fig. 1, the hybridly polarized vector fields have the rich SoP (including linear polarization, right-handed (RH) and left-handed (LH) elliptical polarizations) in the cross section of the field. Generally, the Poincaré sphere is adopted to visualize the distribution of SoP. For the azimuthal-variant hybridly polarized vector field, its Stokes parameters are only dependent on the azimuthal angle and the SoP spans complete meridians on the surface of the Poincaré sphere [20]. For the radial-variant hybridly polarized vector field or the spatial-variant hybridly polarized vector field, however, the SoP representation should use the radius-dependent Poincaré sphere because its Stokes parameters are dependent on both the azimuthal angle and the radial position.

3 Focusing properties of hybridly polarized vector fields

For the spatial-variant hybridly polarized vector field described by Eq. (1), its pupil function along the x and y axes can be written as

$$A_x(\theta, \phi) = A_0 P(\theta) \exp\left[i(m\phi + 2\pi n\beta^2 \left(\frac{\sin \theta}{\sin \alpha}\right)^2 + \varphi_0)\right], \tag{2}$$

$$A_y(\theta, \phi) = A_0 P(\theta) \exp\left[-i(m\phi + 2\pi n\beta^2 \left(\frac{\sin \theta}{\sin \alpha}\right)^2 + \varphi_0)\right], \tag{3}$$

where β is the pupil filling factor defined as the ratio of the pupil radius to the beam waist, and $P(\theta)$ is the pupil apodization function. For a uniform-intensity illumination, $P(\theta) = \text{circ}(\beta \sin \theta / \sin \alpha)$ is chosen in the entire analysis in this work.

According to the vectorial Debye theory, the electric field in the focal region of an aplanatic lens can be expressed as [28]

$$E_x(\rho, \varphi, z) = -\frac{if}{\lambda} \int_0^\alpha \int_0^{2\pi} \sin \theta \sqrt{\cos \theta} e^{ik[z \cos \theta + \rho \sin \theta \cos(\phi - \varphi)]} \times [A_x(\theta, \phi)(\cos^2 \phi \cos \theta + \sin^2 \phi) + A_y(\theta, \phi) \cos \phi \sin \phi (\cos \theta - 1)] d\theta d\phi, \tag{4}$$

$$E_y(\rho, \varphi, z) = -\frac{if}{\lambda} \int_0^\alpha \int_0^{2\pi} \sin \theta \sqrt{\cos \theta} e^{ik[z \cos \theta + \rho \sin \theta \cos(\phi - \varphi)]} \times [A_x(\theta, \phi) \cos \phi \sin \phi (\cos \theta - 1) + A_y(\theta, \phi)(\cos^2 \phi + \sin^2 \phi \cos \theta)] d\theta d\phi, \tag{5}$$

$$E_z(\rho, \varphi, z) = -\frac{if}{\lambda} \int_0^\alpha \int_0^{2\pi} \sin^2 \theta \sqrt{\cos \theta} e^{ik[z \cos \theta + \rho \sin \theta \cos(\phi - \varphi)]} \times [A_x(\theta, \phi) \cos \phi + A_y(\theta, \phi) \sin \phi] d\theta d\phi, \tag{6}$$

where ρ , φ , and z are the polar radius, azimuthal angle, and longitudinal position in the cylindrical coordinate system for the observation point, respectively; $k = 2\pi/\lambda$ is the wave number, f is the focal length of the objective lens, λ is the wavelength, and $\alpha = \arcsin(\text{NA})$ is the maximal angle yielded by the NA of the objective lens.

Substituting Eqs. (2) and (3) into Eqs. (4)–(6), after tedious mathematical reduction, the electric field in the vicinity of focus can be found as

$$E_x(\rho, \varphi, z) = c_0 i^{m-1} \int_0^\alpha \sin \theta \sqrt{\cos \theta} P(\theta) e^{ikz \cos \theta} \{ (1 + \cos \theta) J_m(\xi) e^{i\Psi} + \frac{(1 - \cos \theta)}{2} [J_{m+2}(\xi) e^{i(\Psi+2\varphi)} + J_{m-2}(\xi) e^{i(\Psi-2\varphi)} + iJ_{m+2}(\xi) e^{-i(\Psi+2\varphi)} - iJ_{m-2}(\xi) e^{-i(\Psi-2\varphi)}] \} d\theta, \tag{7}$$

$$E_y(\rho, \varphi, z) = c_0 i^{m-1} \int_0^\alpha \sin \theta \sqrt{\cos \theta} P(\theta) e^{ikz \cos \theta} \{ (1 + \cos \theta) J_m(\xi) e^{-i\Psi} - \frac{(1 - \cos \theta)}{2} [J_{m+2}(\xi) e^{-i(\Psi+2\varphi)} + J_{m-2}(\xi) e^{-i(\Psi-2\varphi)} + iJ_{m+2}(\xi) e^{i(\Psi+2\varphi)} - iJ_{m-2}(\xi) e^{i(\Psi-2\varphi)}] \} d\theta, \tag{8}$$

$$E_z(\rho, \varphi, z) = c_0 i^m \int_0^\alpha \sin^2 \theta \sqrt{\cos \theta} P(\theta) e^{ikz \cos \theta} \times [J_{m+1}(\xi) e^{i(\Psi+\varphi)} - J_{m-1}(\xi) e^{i(\Psi-\varphi)} + iJ_{m+1}(\xi) e^{-i(\Psi+\varphi)} + iJ_{m-1}(\xi) e^{-i(\Psi-\varphi)}] d\theta, \tag{9}$$

with $\xi = k\rho \sin \theta$, $\Psi = m\varphi + 2\pi n\beta^2 (\sin \theta / \sin \alpha)^2 + \varphi_0$, and $c_0 = \pi A_0 f / \lambda$. Here, $J_m(x)$ is the m th order Bessel function of the first kind. Equations (7)–(9) are the basic

result of the present work, which provides a general expression for the electric components in the focal region of a spatial-variant hybridly polarized vector field. Note that the focal field of a radial-variant hybridly polarized vector field is obtained by setting $m = 0$ in Eqs. (7)–(9), which is consistent with the one reported previously [25].

3.1 Low-NA focusing of hybridly polarized vector fields

With the above results, we first investigate the focusing property and the polarization evolution of the hybridly polarized vector fields focused under low-NA condition both theoretically and experimentally. The generated vector fields are focused by an $\text{NA} = 0.17$ objective lens with a focal length of 150 mm. The parameters of the focusing lens are chosen such that a detector (Beamview, Coherent Inc.) can probe a region-of-interest field in the entire focal region. It should be noted that the longitudinal field becomes negligible compared with the transverse field for the low-NA case. Accordingly, the longitudinal component of the focal field (Eq. 9) can be safely omitted for the analysis.

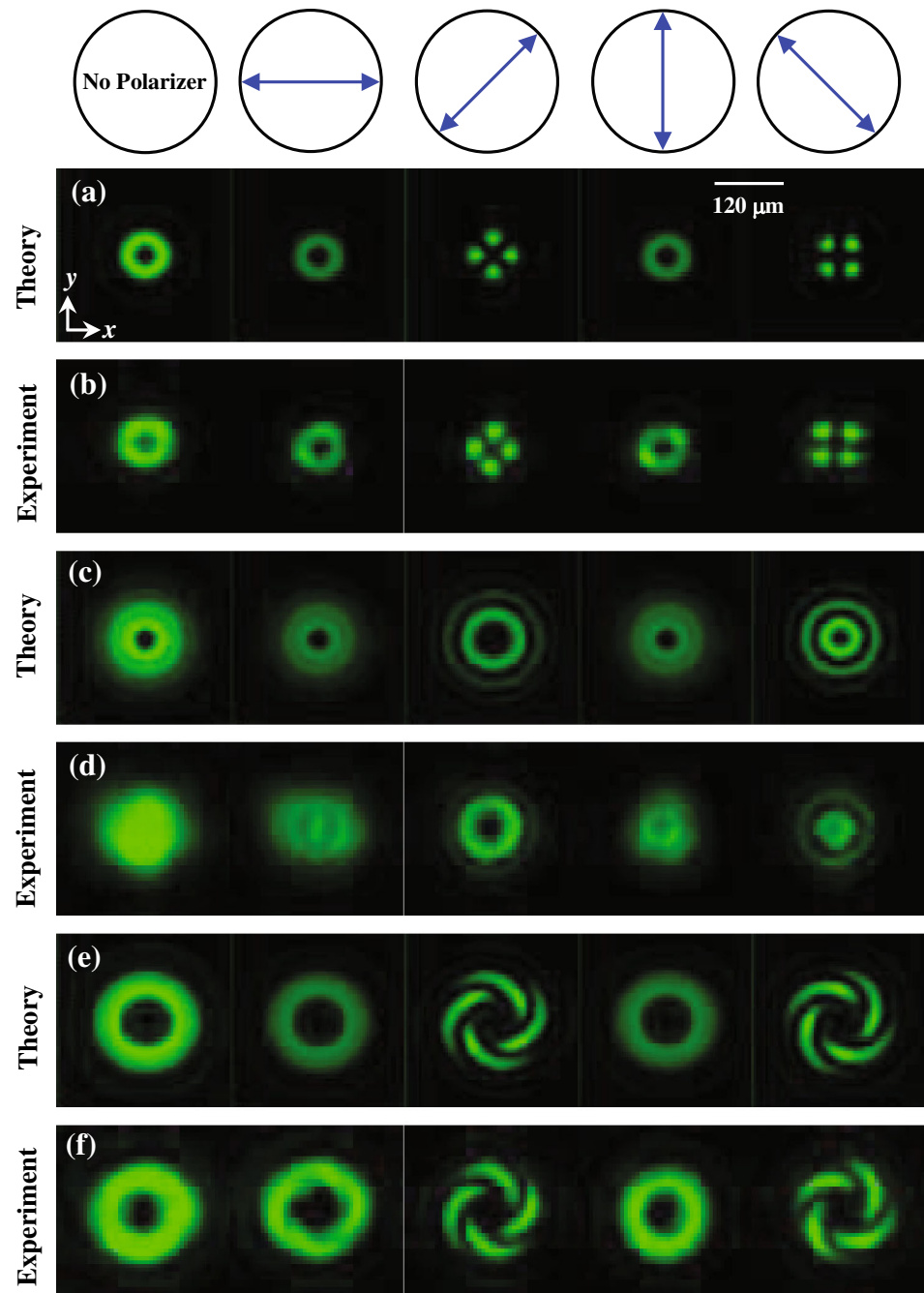
Figure 2 shows the intensity patterns of hybridly polarized vector fields at the geometrical focal plane of the low-NA lens when $\lambda = 532$ nm, $\beta = 15$, $\text{NA} = 0.17$, and $\varphi_0 = 0$. To identify the vector behavior of the focused field, a linear polarizer is used and the corresponding simulated and measured transverse intensity patterns are displayed. The measured results are consistent with the numerical simulations. Without the polarizer, the focal fields of the hybridly polarized vector fields exhibit the doughnut profile with a central dark spot, as displayed in the first column of Fig. 2. When a linear polarizer is used, the extinction behaviors of the focal fields are similar to those of the input fields shown in Fig. 1. Note that the chirality of the extinction spiral for the spatial-variant hybridly polarized vector field after a $\pi/4$ and $3\pi/4$ linear polarizers (see Fig. 2e) exhibits a LH screw orientation, different from that of the input field (see Fig. 1d). This result is similar to that reported for the spatial-variant linearly polarized vector field [11] and can be understood as the following. In general, the polarization orientations of the optical field on two sides of the geometrical focal plane are orthogonal to each other opposite, due to the bifocusing behavior of the spatial-variant hybridly polarized vector field (see the first row of Fig. 5). For the spatial-variant hybridly polarized vector field after a $\pi/4$ linear polarizer in front of the lens and before the first focus, its extinction spiral is a RH screw orientation (see Fig. 1d). Between the two foci and near the geometrical focal plane, the extinction spiral turns to a LH screw. That is, the chirality of the extinction spiral for the spatial-variant hybridly polarized

vector field after a $\pi/4$ or $3\pi/4$ linear polarizer at the geometrical focal plane (see Fig. 2e) exhibits a LH screw orientation. After the second focus and further down the optical axis, the intensity pattern after passing a $\pi/4$ or $3\pi/4$ linear polarizer shows the extinction spiral with a RH screw orientation (see Fig. 5).

To illustrate the propagation behavior of the azimuthal-variant hybridly polarized vector field, numerical simulations have been performed using Eqs. (7)–(9) with $n = 0$, $\lambda = 532$ nm, $\beta = 15$, and $\text{NA} = 0.17$. Figure 3 shows the intensity distributions of a vector field with $m = 2$ and $\varphi_0 = 0$ through the focal region of the lens. Figure 3a displays the simulated intensity pattern through the lens' geometrical focus in the YZ plane ($x = 0$). Clearly, the focused vector field forms a doughnut field with a central dark spot. Setting $n = 0$ in Eqs. (7) and (8), one finds that the intensities along the x and y components are independent of the azimuthal angle φ , suggesting that the transverse intensity holds the cylindrical symmetry at any propagation position. Figure 3b, c shows the measured and simulated transverse intensity patterns taken at planes (1 \rightarrow 5) with the separation of $d = 6.25$ mm marked in Fig. 3a, respectively. The corresponding intensity patterns after passing a $\pi/4$ linear polarizer are displayed in Fig. 3d, e. Clearly, the experimental results are in good agreement with the numerical simulations. By calculating the Stokes parameters, we map the distribution of SoP at their planes (shown in Fig. 3e). The focal field at different planes exhibits hybrid SoP. More importantly, the focused field of the azimuthal-variant hybridly polarized vector fields preserves the initial polarization at any propagation position.

The focusing property of radial-variant hybridly polarized vector fields under low-NA condition are studied with Eqs. (7)–(9) for $m = 0$ and shown in Fig. 4. One can see that the transverse intensity $I_T = |E_x|^2 + |E_y|^2$ is independent of the azimuthal angle φ , indicating that the transverse intensity preserves the cylindrical symmetry at any propagation position. Figure 4 shows the intensity distributions of the radial-variant hybridly polarized vector field in the focal region when $\lambda = 532$ nm, $\beta = 15$, $n = 1$, and $\text{NA} = 0.17$. Both the measured and simulated results indicate that the focal field of the radial-variant hybridly polarized vector field exhibits a bifocusing behavior along the optical axis, similar to that of a radial-variant linearly polarized vector field [19]. This phenomenon can be easily understood by inspecting Eq. (1). For $n > 0$, the radial-dependent terms of the phase for the x -polarized and y -polarized components can be regarded as equivalent to lens functions with opposite powers. After the lens, the y -polarized component will be focused in front of the geometrical focal plane with the x -polarized component being focused behind the geometrical focal plane. Consequently, the focused radial-variant vector

Fig. 2 Theoretically predicted and experimentally measured intensity patterns of various hybridly polarized vector fields at the geometrical focal plane ($\lambda = 532$ nm, $\beta = 15$, NA = 0.17, and $\varphi_0 = 0$). **a, b** $m = 2$ and $n = 0$; **c, d** $m = 0$ and $n = 1$; and **e, f** $m = 2$ and $n = 1$



fields with hybrid SoP exhibit bifocal behavior along the optical axis. The distributions of SoP at planes (1 \rightarrow 5) marked in Fig. 4a are displayed in Fig. 4e. The polarization evolution of the focused radial-variant hybridly polarized vector field demonstrates some salient features: (1) the distributions of SoP preserve the radial symmetry at any propagation position and (2) the direction of the SoP distributions are nearly orthogonal with respect to the geometrical focal plane.

The intensity distribution and polarization evolution of spatial-variant hybridly polarized vector field focused

under the low-NA illumination condition are studied with the parameters as $\lambda = 532$ nm, $\beta = 15$, NA = 0.17, $m = 2$, $n = 1$, and $\varphi_0 = 0$. As displayed in Fig. 5a, the focused vector field forms an optical bottle-shaped profile with zero on-axis intensity surrounded by regions of higher intensity. The measured intensity patterns (see Fig. 5b, d) are in good agreement with the simulated results (see Fig. 5c, e). Recently, it has been demonstrated that an optical bottle field generated by focused spatial-variant linearly polarized vector field is controllable through tuning the azimuthal and radial indexes [11]. Analogously, the

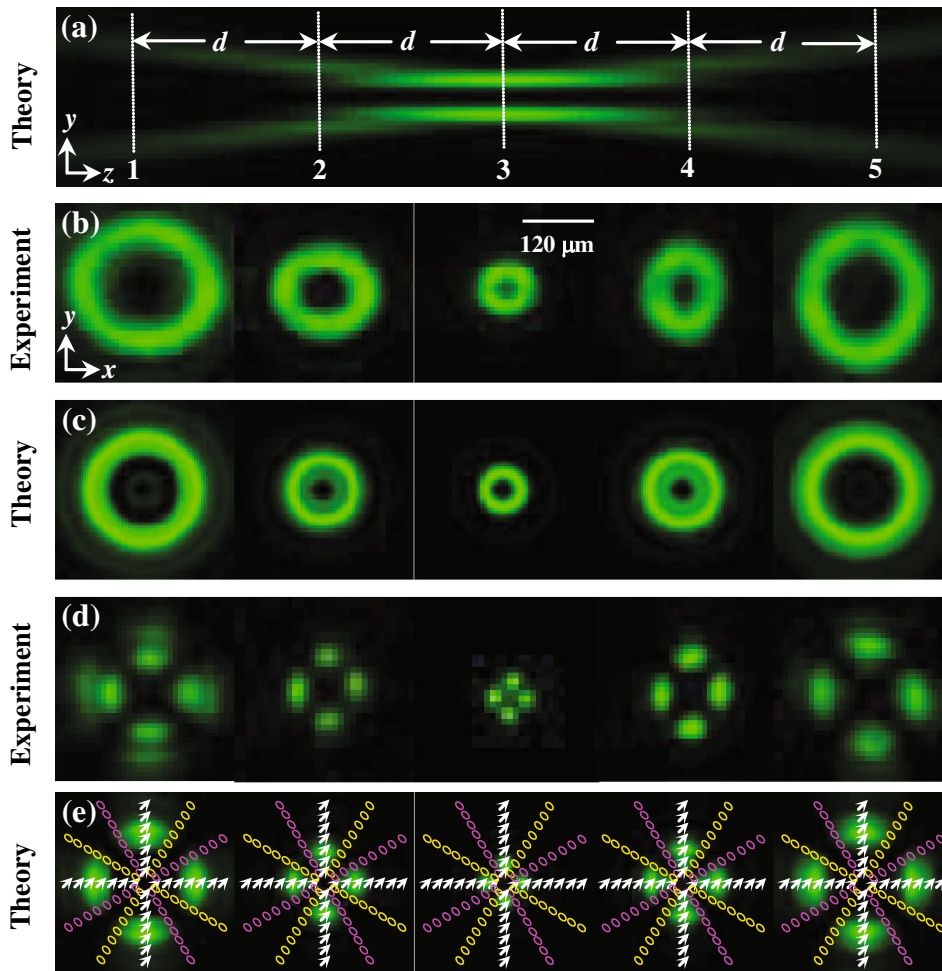


Fig. 3 Intensity distributions of the focused azimuthal-variant hybridly polarized vector field for $\lambda = 532$ nm, $\beta = 15$, $\text{NA} = 0.17$, $m = 2$, $n = 0$, and $\varphi_0 = 0$. **a** Intensity pattern through the focus in the YZ plane with a dimension of $30 \text{ mm} \times 300 \mu\text{m}$. **b–e** The measured and simulated intensity patterns (after a $\pi/4$ linear polarizer) at planes

(1 \rightarrow 5) with separation of $d = 6.25$ mm marked in **(a)**, respectively. The *fifth* row also shows the distribution of SoP (purple RH polarization; yellow LH polarization; white arrows linear polarization) at planes marked in **(a)**

controllable bottle-shaped field is generated easily by focusing the spatial-variant hybridly polarized vector fields with tunable values of m and n . The bottle-shaped field exhibits complicated evolution of SoP at different planes, as shown in Fig. 5e. The focused spatial-variant hybridly polarized vector field has the distribution of azimuthal and radial hybrid SoP with fourfold rotation symmetry. Furthermore, the distributions of SoP on both sides of the geometrical focal plane are nearly orthogonal to each other. In addition, the polarization distribution of the generated bottle-shaped field is controllable by altering the azimuthal and radial indexes.

3.2 High-NA focusing of hybridly polarized vector fields

In this subsection, the tight focusing properties and polarization evolutions of hybridly polarized vector fields

under high-NA condition are investigated numerically. The fixed parameters for the calculations are $c_0 = 1$ and $\varphi_0 = 0$. All intensity patterns shown in Figs. 6, 7, and 8 are normalized to the maximum of the total intensity $I = |E_x|^2 + |E_y|^2 + |E_z|^2$.

Firstly, we study the intensities of the tightly focused azimuthal-variant hybridly polarized vector fields for different values of m and φ_0 using Eqs. (7)–(9) for $n = 0$. For an example, Fig. 6 illustrates the intensity and polarization distributions in the focal region projected onto three orthogonal planes (XY , XZ and YZ planes, respectively) of the azimuthal-variant hybridly polarized vector field when $\text{NA} = 0.8$, $\beta = 1.0$, and $m = 2$. As shown in Fig. 6, the 3D polarization in the focal volume exhibits complex elliptical polarization. The azimuthal-variant hybridly polarized vector field is tightly focused into a flower-like intensity pattern with a hollow spot, similar to that of the azimuthal-

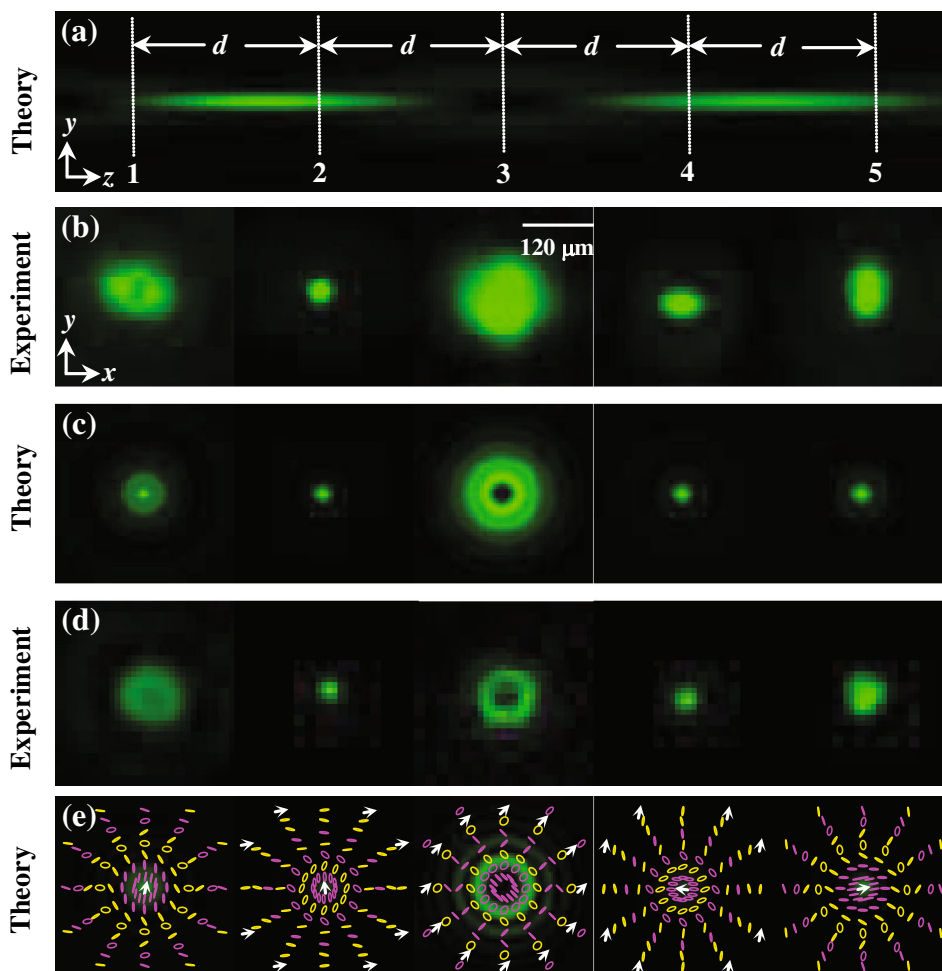


Fig. 4 Intensity distributions of the focused radial-variant hybridly polarized vector field for $\lambda = 532 \text{ nm}$, $\beta = 15$, $\text{NA} = 0.17$, $n = 1$, $m = 0$, and $\varphi_0 = 0$. **a** Intensity pattern through the focus in the YZ plane with a dimension of $30 \text{ mm} \times 30 \mu\text{m}$. **b–e** The measured and simulated intensity patterns (after a $\pi/4$ linear polarizer) at planes

(1 \rightarrow 5) with separation of $d = 6.25 \text{ mm}$ marked in **(a)**, respectively. The *fifth* row also shows the SoP distributions (purple RH polarization; yellow LH polarization; white arrows linear polarization) at planes marked in **(a)**

variant linearly polarized vector field [29]. Furthermore, the radius of the hollow spot increases with increasing the azimuthal index m . In addition, it is found that the intensity distribution in the focal region is nearly independent of φ_0 . It should be emphasized that the focal field of the tightly focused spatial-variant hybridly polarized vector field has 3D elliptical polarization, different from the 3D linear polarization of the spatial-variant linearly polarized vector field [30].

Figure 7 illustrates the intensity and polarization distributions in the focal region projected onto three orthogonal planes of a radial-variant hybridly polarized vector field with $\text{NA} = 0.8$, $\beta = 1.0$, and $n = 1$. It can be seen that the intensity pattern at the geometrical focal plane (XY plane) exhibits a ring shape, which is consistent with the previously reported results [23]. Numerical simulation indicates

that the radius of the focal ring increases as the radial index n increases. As shown in Fig. 7, the intensity of the radial-variant hybridly polarized vector field in the XZ (or YZ) plane has two foci along the optical axis sandwiching a dark region around the geometrical focus. From the 3D polarization projection shown in Fig. 7, it can be seen that one of the focal spot is predominantly x -polarized with the other one predominantly y -polarized, which is consistent with the analysis in Sect. 3.1.

The focal field distribution of a spatial-variant hybridly polarized vector field will have characteristics in combination of the azimuthal-variant hybridly polarized vector field having the flower-like pattern and the radial-variant hybridly polarized vector field exhibiting the bifocal behavior through the focus. Accordingly, the tightly focused spatial-variant hybridly polarized vector field

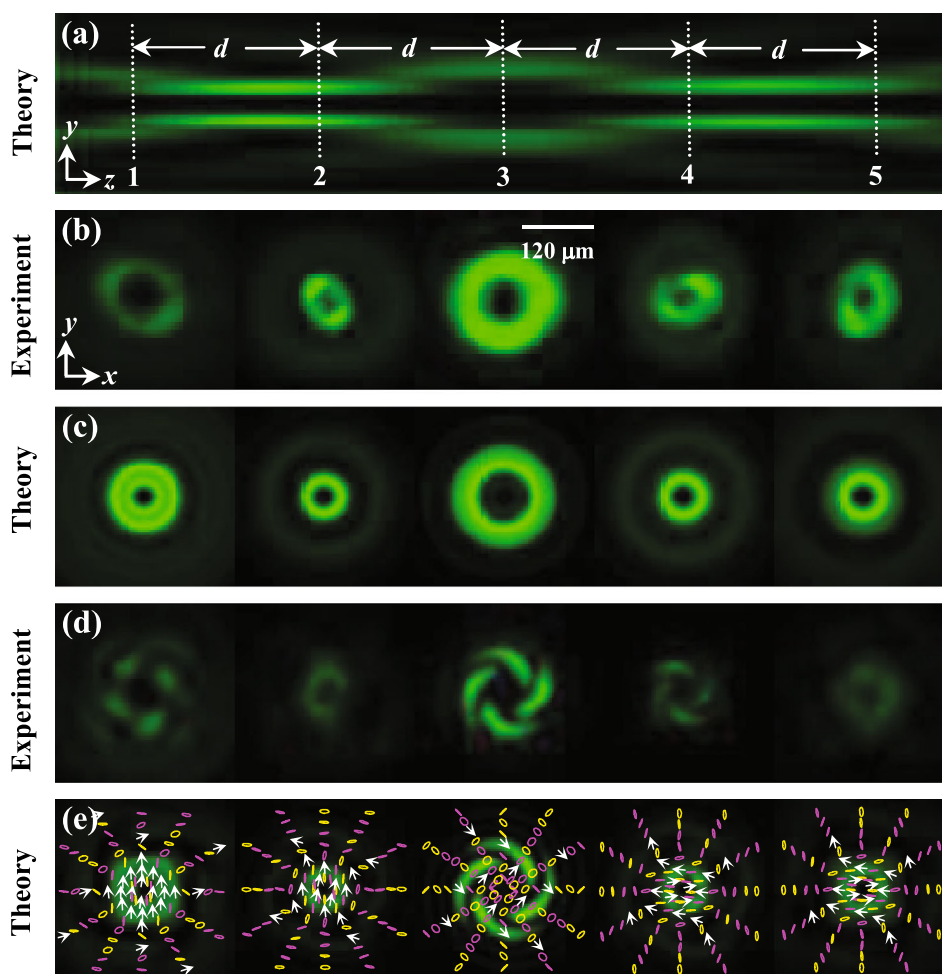


Fig. 5 Intensity distributions of the focused spatial-variant hybridly polarized vector field for $m = 2$, $n = 1$, $\varphi_0 = 0$, $\lambda = 532$ nm, $\beta = 15$, and $\text{NA} = 0.17$. **a** Intensity pattern through the focus in the YZ plane with a dimension of $30 \text{ mm} \times 30 \mu\text{m}$. **b–e** The measured and simulated intensity patterns (after a $\pi/4$ linear polarizer) at planes

(1 \rightarrow 5) with separation of $d = 6.25$ mm marked in **(a)**, respectively. The *fifth* row also shows the distributions of SoP (purple RH polarization; yellow LH polarization; white arrows linear polarization) at planes marked in **(a)**

exhibits an abundant focal volume shape. For instance, Fig. 8 illustrates the intensity and 3D polarization distributions of the tightly focused vector field with $m = 2$ and $n = 1$. Obviously, the focused vector field forms an optical bottle-shaped field with zero on-axis intensity surrounded by a cylindrical light wall. It should be noted that this bottle-shaped field shows an interesting polarization distribution with 3D orientation and space variant ellipticity. Moreover, one could easily modify both the intensity patterns and 3D polarization distributions in the focal region by tuning the azimuthal and radial indexes.

It should be emphasized that the focal field distributions presented here are under moderately high-NA. Numerical simulations indicate that the contribution of the longitudinal component in the total intensity increases with increasing the value of NA. It is found that the polarization distribution nearly along the optical axis will emerge in the

extreme high-NA case although the intensity patterns remain almost unchanged.

4 Optical curl forces on Rayleigh particles induced by tightly focused hybridly polarized vector fields

In Sect. 3, we demonstrated the controllable focal volume and 3D polarization distribution of tightly focused spatial-variant hybridly polarized vector fields, which has the intriguing applications in particle orientation analysis [6, 20, 31, 32], controllable field collapse [4], and particle trapping and manipulation [23, 24]. Traditionally, optical forces on Rayleigh particles are divided into two contributions: the gradient force and the scattering (or radiation pressure) force. The gradient force is proportional to the gradient of the optical intensity and pulls the particles

Fig. 6 Projections of the intensity and polarization distributions (*blue* LH polarization; *green* RH polarization) in the focal region onto three orthogonal planes of the azimuthal-variant hybridly polarized vector field when $\text{NA} = 0.8$, $\beta = 1.0$, $m = 2$, and $n = 0$

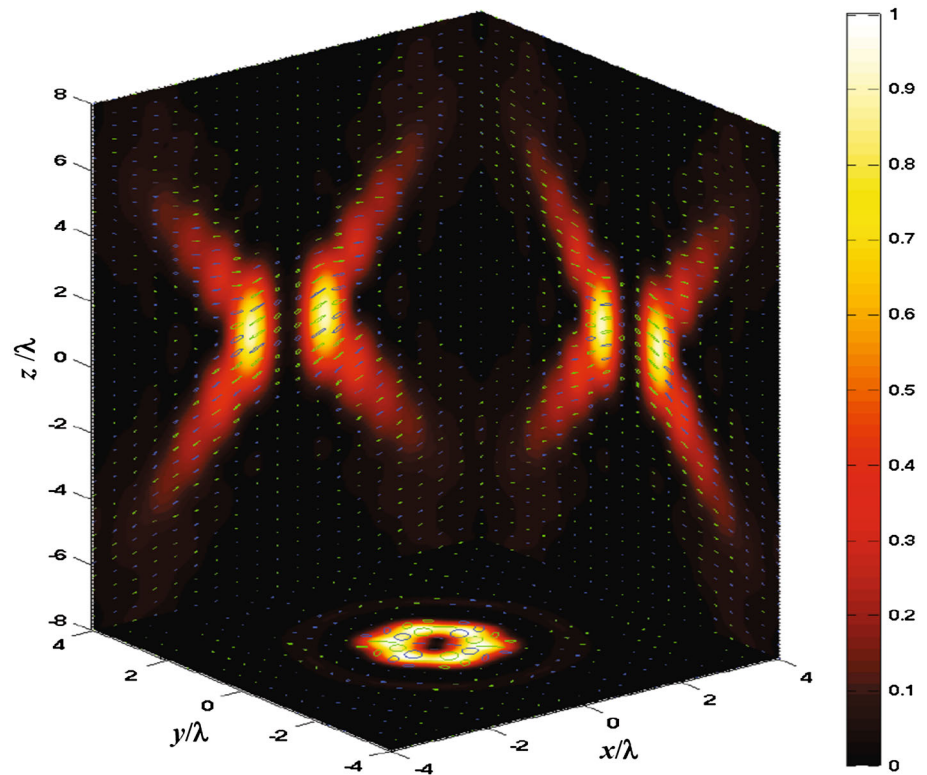
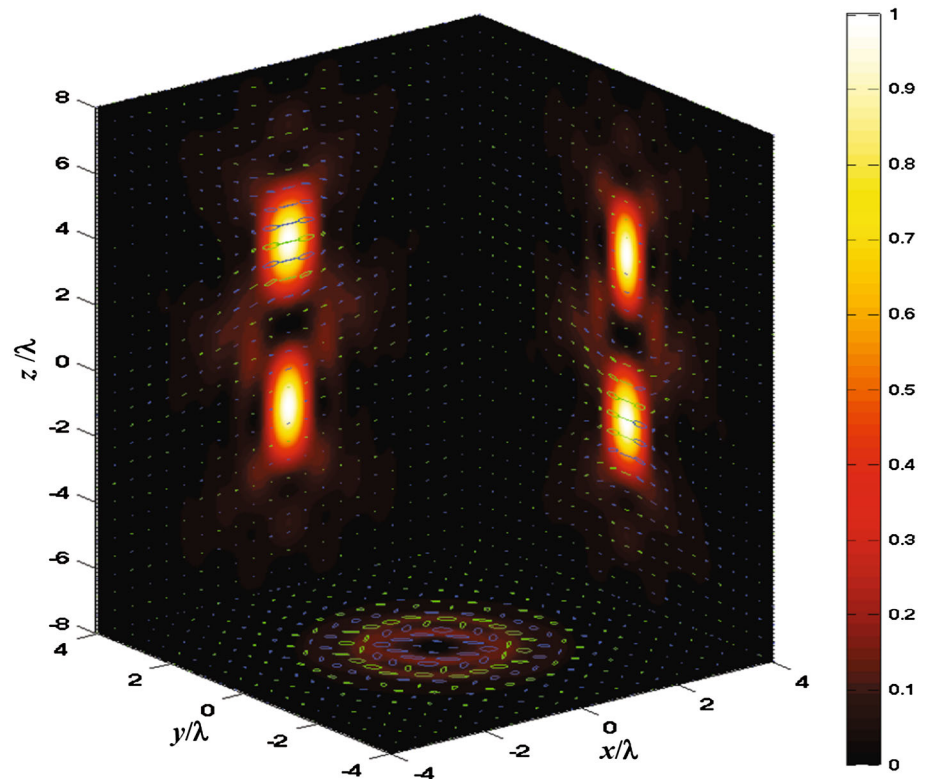


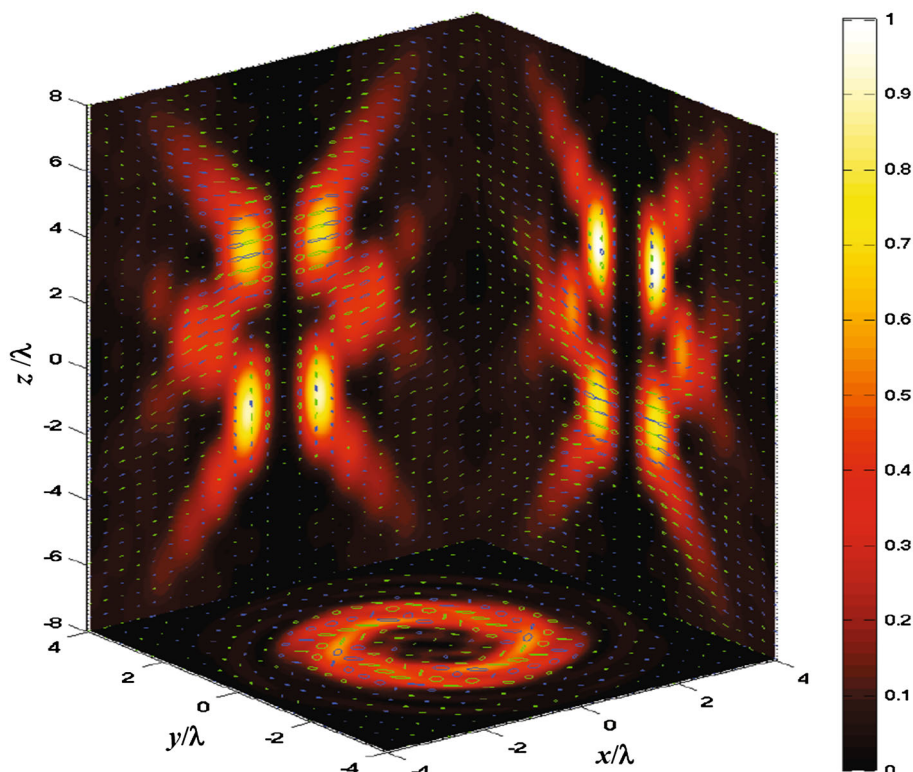
Fig. 7 Projections of the intensity and polarization distributions (*blue* LH polarization; *green* RH polarization) in the focal region onto three orthogonal planes of the radial-variant hybridly polarized vector field when $\text{NA} = 0.8$, $\beta = 1.0$, $m = 0$, and $n = 1$



toward the center of focus. However, the scattering force is proportional to the Poynting vector and tends to push the particles out of focus. By fashioning the proper optical field

gradient, it is possible to trap and manipulate Rayleigh particles with optical tweezers [33]. For many scalar light fields and linearly polarized vector fields, such as

Fig. 8 Projections of the intensity and SoP distributions (blue LH polarization; green RH polarization) in the focal region onto three orthogonal planes of the hybridly polarized vector field when $NA = 0.8$, $\beta = 1.0$, $m = 2$, and $n = 1$



anomalous hollow beams [34] and radially polarized beams [1], the usual gradient and scattering light forces provide the well-known descriptions.

Recently, one has found that a so-called curl force originated from the curl of the light angular momentum [35] plays an important role in determining the resultant optical forces on manometer-sized absorbing particles [24]. For the sake of simplicity, we consider only the light curl force on Rayleigh particles induced by tightly focused hybridly polarized vector fields. For continuous-wave harmonic vector light fields, this optical curl force can be expressed by [35]

$$\mathbf{F}_{\text{curl}} = \frac{1}{2} \text{Im}(\alpha') \text{Im}[(\mathbf{E}^* \cdot \nabla) \mathbf{E}]. \quad (10)$$

Here the complex polarizability α' is given by [36]

$$\alpha' = \frac{\alpha_0}{1 - i\alpha_0 k'^3 / (6\pi\epsilon_0)}, \quad \alpha_0 = 4\pi\epsilon_0 a^3 \frac{(n_1/n_2)^2 - 1}{(n_1/n_2)^2 + 2}, \quad (11)$$

where ϵ_0 is the vacuum's permittivity, a is the radius of spherical particle, n_1 is the refractive index of particles, $k' = kn_2$ is the wave number in a surrounding medium (liquid) of the refractive index n_2 .

Using Eqs. (7)–(11), one can calculate the light curl force on a Rayleigh dielectric sphere produced by tightly focused spatial-variant hybridly polarized vector fields.

Without loss of generality, we take the parameters as $NA = 0.8$, $r_0 = 2$ mm, $\beta = 1$, $\lambda = 532$ nm, $a = 50$ nm, $n_1 = 1.6$, $n_2 = 1.33$ (for water), and the laser beam power $P_0 = 1$ W. Figure 9 shows the magnitude and direction distributions of the curl force at the lens' focal plane for the hybridly polarized vector fields. As displayed in Fig. 9, the magnitude of curl force for the azimuthal-variant hybridly polarized vector field is one order of magnitude greater than that for the radial-variant hybridly polarized vector field. While the magnitude of curl force for the spatial-variant hybridly polarized vector field can be regarded as the coupling between that for the azimuthal- and radial-variant hybridly polarized vector fields. Besides, the transverse curl forces may demonstrate as the swirling force. Interestingly, the direction of curl force produced by the radial-variant hybridly polarized vector field for $n > 0$ is mainly manifesting the clockwise direction, contrast to the anticlockwise direction for $n < 0$. In the trapping experiments using the tightly focused radial-variant hybridly polarized vector field, the motion direction of the trapped particles is synchronously reversed when the radial index n is switched from positive to negative. The results have been validated by the reported experiments [23]. Besides, we also calculate the transverse curl forces produced by the radial-variant linearly polarized vector field and find that it is negligible. Consequently, for the particles trapped in the ring optical tweezers produced by radial-

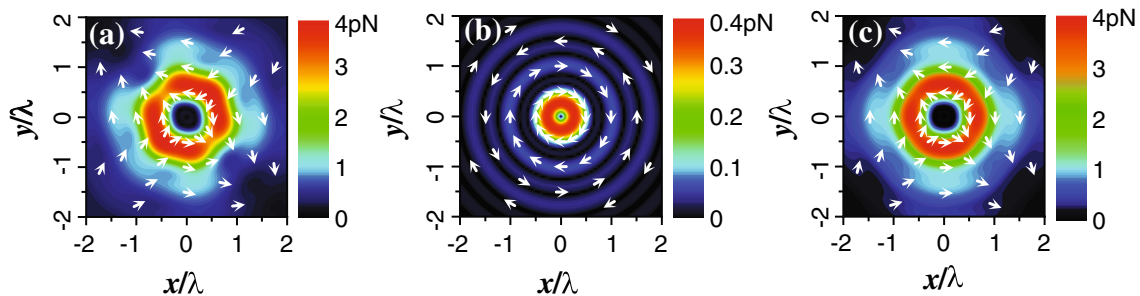


Fig. 9 Transverse curl forces at the plane of $z = 0$ for hybridly polarized vector fields with **a** $m = 2$ and $n = 0$, **b** $m = 0$ and $n = 1$, and **c** $m = 2$ and $n = 1$. Other parameters are $n_1 = 1.6$, $n_2 = 1.33$, $a = 50$ nm, $\lambda = 532$ nm, $P_0 = 1$ W, NA = 0.8, $r_0 = 2$ mm, $\beta = 1$, and $\phi_0 = 0$

variant linearly polarized vector fields, no motion is observed around the ring focus [23].

5 Conclusions

In summary, we have investigated both theoretically and experimentally the focusing property and polarization evolution characteristics of focused hybridly polarized vector fields. Three types of hybridly polarized vector fields, namely azimuthal-variant hybridly polarized vector field, radial-variant hybridly polarized vector field, and spatial-variant hybridly polarized vector field, are successfully generated by a common path interferometer implemented with a SLM. The focal field of the focused hybridly polarized vector fields is studied with the vectorial diffraction method. The intensity distributions and the polarization evolution of the hybridly polarized vector fields focused with low-NA lens are studied experimentally. Good agreements between the numerical simulations and experimental results are obtained. The 3D polarization and 3D intensity distributions near the focus of a high-NA objective lens using these hybridly polarized vector fields as illumination are numerically studied. It is found that the focal field of highly focused azimuthal-variant hybridly polarized vector field exhibits a flower-like pattern, while the focal field of a tightly focused radial-variant hybridly polarized vector field exhibiting a bifocal behavior, and a highly focused spatial-variant hybridly polarized vector field forming an optical bottle-shaped distribution. Furthermore, the focal regions of the tightly focused hybridly polarized vector fields show very complex and interesting polarization distributions with 3D orientation and space variant ellipticity. The optical curl force on Rayleigh particles induced by tightly focused hybridly polarized vector fields, which results in the orbital motion of trapped particles, is analyzed. The intensity distributions and 3D polarization distributions of these focused spatial-variant hybridly polarized vector fields are controllable through adjusting the parameters of

the phase modulation, which may find intriguing applications in particle orientation analysis [6, 20, 31, 32], controllable field collapse [4], particle trapping and manipulation [23, 24].

Acknowledgments This work was supported by the National Science Foundation of China (Grant: 11174160) and the Program for New Century Excellent Talents in University (NCET-10-0503).

References

1. Q. Zhan, Trapping metallic Rayleigh particles with radial polarization. *Opt. Express* **12**, 3377–3382 (2004)
2. C. Hnatovsky, V. Shvedov, W. Krolikowski, A. Rode, Revealing local field structure of focused ultrafast pulses. *Phys. Rev. Lett.* **106**, 123901 (2011)
3. G. Bautista, M.J. Huttunen, J. Mäkitalo, J.M. Kontio, J. Simonen, M. Kauranen, Second-harmonic generation imaging of metal nano-objects with cylindrical vector beams. *Nano Lett.* **12**, 3207–3212 (2012)
4. S.M. Li, Y. Li, X.L. Wang, L.J. Kong, K. Lou, C. Tu, Y. Tian, H.T. Wang, Taming the collapse of optical fields. *Sci. Rep.* **2**, 1007 (2012)
5. J.T. Barreiro, T.C. Wei, P.G. Kwiat, Remote preparation of single-photon “hybrid” entangled and vector-polarization states. *Phys. Rev. Lett.* **105**, 030407 (2010)
6. L. Novotny, M.R. Beversluis, K.S. Youngworth, T.G. Brown, Longitudinal field modes probed by single molecules. *Phys. Rev. Lett.* **86**, 5251–5254 (2001)
7. K.G. Lee, H.W. Kihm, J.E. Kihm, W.J. Choi, H. Kim, C. Ropers, D.J. Park, Y.C. Yoon, S.B. Choi, D.H. Woo, J. Kim, B. Lee, Q.H. Park, C. Lienau, D.S. Kim, Vector field microscopic imaging of light. *Nat. Photon.* **1**, 53–56 (2007)
8. X. Li, T.H. Lan, C.H. Tien, M. Gu, Three-dimensional orientation-unlimited polarization encryption by a single optically configured vectorial beam. *Nat. Commun.* **3**, 998 (2012)
9. K.S. Youngworth, T.G. Brown, Focusing of high numerical aperture cylindrical-vector beams. *Opt. Express* **7**, 77–87 (2000)
10. Q.W. Zhan, Cylindrical vector beams: from mathematical concepts to applications. *Adv. Opt. Photon.* **1**, 1–57 (2009)
11. B. Gu, J.L. Wu, Y. Pan, Y. Cui, Controllable vector bottle-shaped fields generated by focused spatial-variant linearly polarized vector beams. *Appl. Phys. B* **113**, 165–170 (2013)
12. J. Arlt, M.J. Padgett, Generation of a beam with a dark focus surrounded by regions of higher intensity: the optical bottle beam. *Opt. Lett.* **25**, 191–193 (2000)

13. Y. Kozawa, S. Sato, Focusing property of a double-ring-shaped radially polarized beam. *Opt. Lett.* **31**, 820–822 (2006)
14. X.L. Wang, J. Ding, J.Q. Qin, J. Chen, Y.X. Fan, H.T. Wang, Configurable three-dimensional optical cage generated from cylindrical vector beams. *Opt. Commun.* **282**, 3421–3425 (2009)
15. Y. Zhao, Q. Zhan, Y. Zhang, Y.P. Li, Creation of a three-dimensional optical chain for controllable particle delivery. *Opt. Lett.* **30**, 848–850 (2005)
16. H.F. Wang, L.P. Shi, B. Lukyanchuk, C. Sheppard, C.T. Chong, Creation of a needle of longitudinally polarized light in vacuum using binary optics. *Nat. Photon.* **2**, 501–505 (2008)
17. K. Hu, Z. Chen, J. Pu, Generation of super-length optical needle by focusing hybridly polarized vector beams through a dielectric interface. *Opt. Lett.* **37**, 3303–3305 (2012)
18. B. Gu, J.L. Wu, Y. Pan, Y. Cui, Achievement of needle-like focus by engineering radial-variant vector fields. *Opt. Express* **21**, 30444–30452 (2013)
19. B. Gu, Y. Pan, J.L. Wu, Y. Cui, Manipulation of radial-variant polarization for creating tunable bifocusing spots. *J. Opt. Soc. Am. A* **31**, 253–257 (2014)
20. G.M. Lerman, L. Stern, U. Levy, Generation and tight focusing of hybridly polarized vector beams. *Opt. Express* **18**, 27650–27657 (2010)
21. X.L. Wang, Y.N. Li, J. Chen, C.S. Guo, J.P. Ding, H.T. Wang, A new type of vector fields with hybrid states of polarization. *Opt. Express* **18**, 10786–10795 (2010)
22. W. Han, W. Cheng, Q. Zhan, Flattop focusing with full Poincaré beams under low numerical aperture illumination. *Opt. Lett.* **36**, 1605–1607 (2011)
23. X.L. Wang, J. Chen, Y.N. Li, J.P. Ding, C.S. Guo, H.T. Wang, Optical orbital angular momentum from the curl of polarization. *Phys. Rev. Lett.* **105**, 253602 (2010)
24. L.G. Wang, Optical forces on submicron particles induced by full Poincaré beams. *Opt. Express* **20**, 20814–20826 (2012)
25. K. Hu, Z. Chen, J. Pu, Tight focusing properties of hybridly polarized vector beams. *J. Opt. Soc. Am. A* **29**, 1099–1104 (2012)
26. H. Hu, P. Xiao, The tight focusing properties of spatial hybrid polarization vector beam. *Optik* **124**, 2406–2410 (2013)
27. X.L. Wang, J.P. Ding, W.J. Ni, C.S. Guo, H.T. Wang, Generation of arbitrary vector beams with a spatial light modulator and a common path interferometric arrangement. *Opt. Lett.* **32**, 3549–3551 (2007)
28. B. Richards, E. Wolf, Electromagnetic diffraction in optical systems II. Structure of the image field in an aplanatic system. *Proc. R. Soc. A* **253**, 358–379 (1959)
29. M. Rashid, O.M. Maragò, P.H. Jones, Focusing of high order cylindrical vector beams. *J. Opt. A Pure Appl. Opt.* **11**, 065204 (2009)
30. H. Chen, Z. Zheng, B.F. Zhang, J. Ding, H.T. Wang, Polarization structuring of focused field through polarization-only modulation of incident beam. *Opt. Lett.* **35**, 2825–2827 (2010)
31. A.F. Abouraddy, K.C. Toussaint Jr, Three-dimensional polarization control in microscopy. *Phys. Rev. Lett.* **96**, 153901 (2006)
32. W. Chen, Q. Zhan, Diffraction limited focusing with controllable arbitrary three-dimensional polarization. *J. Opt.* **12**, 045707 (2010)
33. A. Ashkin, J.M. Dziedzic, J.E. Bjorkholm, S. Chu, Observation of a single-beam gradient force optical trap for dielectric particles. *Opt. Lett.* **11**, 288–290 (1986)
34. Z. Liu, D. Zhao, Optical trapping Rayleigh dielectric spheres with focused anomalous hollow beams. *Appl. Opt.* **52**, 1310–1316 (2013)
35. S. Albaladejo, M.I. Marqués, M. Laroche, J.J. Sáenz, Scattering forces from the curl of the spin angular momentum of a light field. *Phys. Rev. Lett.* **102**, 113602 (2009)
36. B.T. Draine, The discrete-dipole approximation and its application to interstellar graphite grains. *Astrophys. J.* **333**, 848–872 (1988)